Journal of Colloid and Interface Science 627 (2022) 427–437

Contents lists available at ScienceDirect

Journal of Colloid and Interface Science

journal homepage: www.elsevier.com/locate/jcis

Mechanism of gelation in high nickel content cathode slurries for sodium-ion batteries

Samuel Roberts [a], Lin Chen [b], Brij Kishore [b], Claire E.J. Dancer [a], Mark J.H. Simmons [c], Emma Kendrick [b,*]

[a] WMG, University of Warwick, Coventry CV4 7AL, United Kingdom
[b] School of Metallurgy and Materials, University of Birmingham, B15 2TT, United Kingdom
[c] School of Chemical Engineering, University of Birmingham, Birmingham B15 2TT, United Kingdom

GRAPHICAL ABSTRACT

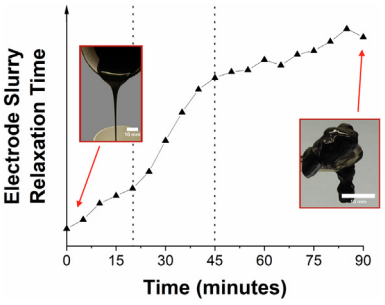

ARTICLE INFO

Article history:
Received 14 April 2022
Revised 17 June 2022
Accepted 5 July 2022
Available online 8 July 2022

Keywords:
Energy storage
Sodium-ion batteries
Layered O3 oxides
Electrode slurry
Gelation

ABSTRACT

Sodium-ion batteries are a prospective sustainable alternative to the ubiquitous lithium-ion batteries due to the abundancy of sodium, and their cobalt free cathodes. The high nickel O3-type oxides show promising energy densities, however, a time dependency in the rheological properties of the composite electrode slurries is observed, which leads to inhomogeneous coatings being produced. A combination of electron microscopy and infra-red spectroscopy were used to monitor the O3-oxide surface changes upon exposure to air, and the effect upon the rheology and stability of the inks was investigated. Upon exposure to air, NaOH rather than Na_2CO_3 was observed on the surfaces of the powder through FTIR and EDS. The subsequent gelation of the slurry was initiated by the NaOH and dehydrofluorination with crosslinking of PVDF was observed through the reaction product, NaF. Approximately 15% of the CF bonds in PVDF undergo this dehydrofluorination to form NaF. As observed in the relaxation time of fitted rheological data, the gelation undergoes a three-stage process: a dehydrofluorination stage, creating saturated structures, a crosslinking stage, resulting in the highest rate of gelation, and a final crosslinking stage. This work shows the mechanism for instability of high nickel containing powders and electrode slurries, and presents a new time dependent oscillatory rheology test that can be used to determine the process window for these unstable slurry systems.

1. Introduction

Whilst lithium-ion batteries are ubiquitously recognised as a panacea for energy storage, having high voltage, long cycle life, and a high specific energy [1,2], their high cost [3] and the reliance

* Corresponding author.
E-mail addresses: s.roberts.7@warwick.ac.uk (S. Roberts), e.kendrick@bham.ac.uk (E. Kendrick).

https://doi.org/10.1016/j.jcis.2022.07.033
0021-9797/

upon critical materials such as graphite, cobalt and lithium [4], have caused alternatives to be sought [5]. Sodium-ion batteries are an emerging technology with a large range of suitable cathode materials available, including transition metal oxides, polyanionic, Prussian blue analogues, and organic cathodes [6,7,16,17,8–15].

An important group among of these suitable materials, which exhibit high specific capacities and high voltages, are transition metal oxides (TMOs) [18], with the general formula Na_xMO_2 ($0 < x \leq 1$, and M refers to a combination of transition metals). TMOs can be categorised further, into *P*2, *P*3, O2, O3, based on the coordination of sodium and the stacking pattern. O refers to an octahedral coordination of oxygens around the sodium and P refers to a prismatic arrangement. The number, 2 and 3, represents the number of layers in the repeating stack [18–20]. Between these, *P*2 and O3 have been the most widely researched, each having their own advantages and disadvantages. When sodium ions are deficient, $x < 1$, it is energetically favourable for the remaining sodium to be in a prismatic environment [18,20]. As *P*2 materials possess a sodium "deficient" state, they remain stable through their cycling range. O3 materials, in comparison, which start in an octahedral coordination, as sodium is removed from their structure, require a phase transition, which can cause low kinetics [18,21]. However, owing to this deficiency, P2 materials typically have lower capacities, whereas O3 oxides, instead, are higher due to higher sodium content, which gives them commercial potential as sodium cathode materials [18,22,23]. Several transition metals have been investigated as substitutes into the M sites due to favourable improvements to the storage or cycling performance [24]. Many transition metals, specifically nickel and cobalt, have been shown to increase the storage capabilities of the material [5,25,26]. However, nickel has additional benefits over cobalt including a lower cost and more sustainable sources. For these reasons, the potential of commercialisation of many high nickel content O3 oxides have been investigated in recent years [24,25].

However, for these materials a significant processing challenge exists. Many layered O3 oxide materials, especially those with a high nickel content, undergo both surface and bulk phase transformations when exposed to air [27], resulting in the formation of sodium residues such as Na_2CO_3 [20] and NaOH [28]. Additionally, exposure to air of electrode slurries containing these layered O3 oxide materials, along with *n*-methyl-2-pyrrolidone (NMP) and poly(vinylidene fluoride) (PVDF) causes them to gel [29,30], which renders the slurries uncoatable and therefore unusable. As a result, careful cathode slurry preparation is required.

The instabilities in the slurries cause variations in the viscosity within minutes of their formulation [5]. It is notable that a similar air sensitivity has been observed in high-nickel content lithium ion cathode materials [31–33], especially in lithium NMC 811 [34–37], and to some extent NMC 622 [34,35,38]. Although several review papers for *lithium* ion batteries have suggested possible reaction routes for the gelation of these cathode inks, no experimental studies exist that elucidate the exact mechanism [39–41].

The work presented here investigates the chemical changes upon the surface of the sodium O3-type layered oxide $NaNi_{1/2}Mn_{1/4}Sn_{1/8}Ti_{1/8}O_2$ cathode materials using a combination of SEM (Scanning Electron Microscopy), EDS (Energy-Dispersive X-ray Spectroscopy), and FTIR (Fourier-Transform Infrared Spectroscopy). The effect of the incorporation of the powder to form an ink, and the time dependent rheology is investigated. A Maxwell model is used to analyse the structural evolution of the electrode slurries during gelation and the chemical changes are monitored through FTIR. Finally, the electrode coatings were studied using XPS (X-ray Photoelectron Spectroscopy) and electrochemical measurement and analysis using half cells.

2. Experimental methods

2.1. Active material synthesis and characterisation

To investigate the gelation effects upon the electrode formulation, 100 g batches of material was synthesised to ensure a consistency in the testing. $NaNi_{1/2}Mn_{1/4}Sn_{1/8}Ti_{1/8}O_2$ (Na-NMST) was synthesised by a solid-state method. Stoichiometric quantities (to produce 100 g of product) of Na_2CO_3, $Ni(NO_3)_2{\cdot}6H_2O$, $MnCO_3$, SnO_2, and TiO_2, (Alfa Aesar, ≥99.5% purity) were ball milled using a Glen Creston roller mill in a 1000 mL HDPE Azlon roller pot. Due to the volatility of sodium during the solid-state synthesis, an extra 5 wt% of Na_2CO_3 was added. A charge of 375 g of 5 mm and 375 g of 10 mm zirconia balls were used for milling. 250 mL of isopropanol (IPA) was initially added, and the pot was milled for more than 48 h to ensure homogeneity. The pressure inside the pot was released every ~30–60 min and, over the course of milling, an extra 200 mL of IPA was added to account for its volatility.

The IPA was removed and condensed under vacuum at approximately 70 °C and the precursor was fired at 900 °C for 24 h. The resulting as-synthesised Na-NMST was transferred hot into a glove box filled with argon to prevent any reaction with air.

Scanning electron microscope (SEM) images of the powder were taken using a Zeiss SUPRA 55-VP with elemental analysis performed using an Oxford Instruments energy-dispersive X-ray (EDS) spectrometer attached to the SEM. SEM images and qualitative elemental analysis were obtained for the as-synthesised material and material placed on SEM stubs that had been exposed to lab air for *ca.* 72 h.

2.2. Electrode slurry formation and characterisation

The active material was milled in a Retsch PM100 Planetary Ball Mill with one third of the total being conductive carbon black (IMERYS, Super C65) to coat the particles and aid in the conductive properties of the electrode. The powders were milled at 300 rpm for 45 min, with a reversal of direction every 15 min. The zirconia balls used had diameters of 5 and 10 mm, with a loading of 45 g and 15 g for the 5- and 10-mm balls, respectively.

Electrode slurries were formed by mixing the carbon coated Na-NMST ($NaNi_{1/2}Mn_{1/4}Sn_{1/8}Ti_{1/8}O_2$) with the remaining conductive carbon black, and an 8 wt% PVDF (polyvinylidene fluoride) (Solvey 5130) binder in NMP (*n*-methyl-2-pyrrolidone) solution in a ratio of 89:6:5 by weight. The cathode ink was mixed in sealed pots in a Thinky ARE-250 planetary mixer, situated in a Munters dry room with a maximum dew point of −40 °C. Materials were measured out under a recirculator hood (also situated in a dry room) or in an argon filled glove box. There were three stages of mixing: initially the active material and the extra NMP, measured to give a final solids content of 40 wt%, followed by the addition of carbon black, and finally, addition of the PVDF solution. Each mixing stage lasted 5 min at a revolution speed of 1300 rpm.

The electrode slurry was chemically characterised using a Bruker Vertex 70v Fourier Transform Infrared spectrometer (FTIR) with a diamond attenuated total reflectance accessory. Data were recorded from 4500 to 100 cm^{-1}, and all measurements were made using 16 scans at 4 cm^{-1} resolution, with appropriate background measurements taken for each spectrum. Measurements were taken every 10 min whilst the slurry was situated on the diamond and exposed to air. The slurry samples were transported to the FTIR spectrometer in sealed vessels following their mixing in the dry room.

Physical measurements of the slurry rheology were obtained using a Malvern Panalytical Pro + rheometer with 40 mm diameter roughened parallel plates and a 1 mm gap. Frequency sweeps were performed, from 0.1 Hz to 100 Hz at two different amplitudes, 0.02% and 0.1%, both of which reside in the linear viscoelastic region (LVER). A constant pre-shear of 10 s^{-1} for 30 s was performed at the start of measurements to eliminate any time dependence in the samples and ensure consistency between results. The frequency sweeps were performed every 5 min on the electrode slurry, between roughened parallel plates. Three repeats were performed.

2.3. Electrode formation and characterisation

Electrodes were formed by coating the electrode slurry onto an aluminium substrate using a doctor blade set at 150 μm, aiming for a target loading of 80 gsm. They were then dried on a hotplate at 80 °C for 40 min, followed by overnight in a vacuum oven at 120 °C. For additional characterisation of the slurry exposure, three different coatings were made from the electrode slurries, one made from the just-mixed slurry (i.e., immediately after mixing), one was coated 20 min after mixing and the final one 40 min after mixing (at which point the slurry gelation was noticeable). All coating was performed inside a recirculator hood situated in a dry room.

X-ray photoelectron spectroscopy (XPS) data on the as-manufactured electrodes was acquired using a Kratos Axis Ultra DLD spectrometer. Samples were transferred to the spectrometer using an airless transfer unit with an argon atmosphere. The surfaces of the samples were found to charge slightly under the X-ray beam during the experiments and to compensate for this, the surfaces were flooded with a beam of low-energy electrons during data acquisition. This in turn required subsequent re-referencing of the data, using the graphitic component of the C1s region at 284.3 eV as the reference point. The data were analysed with the CasaXPS software package, using Shirley backgrounds and mixed Gaussian–Lorentzian (Voigt) line shapes and asymmetry parameters where appropriate.

Cross-section Scanning electron microscopy (SEM) was performed on a Philips XL30 FEG instrument within a holder where the cross-section of the sample facing up, the images are taken under an acceleration voltage of 10 kV. The elemental distributions were measured by energy-dispersive X-ray spectroscopy (EDX, Oxford Inca 300).

Half-cells were assembled in an argon filled glovebox, using sodium metal as the counter (and reference) electrodes, Celgard 2325 and glass fibre (GF/A, Whatman) discs, both cut to 16 mm as dual separators, and the cathode electrodes cut to 14.8 mm. Electrodes had an average thickness of 50.3 μm (±4.3 μm) and an average loading of 77.2 gsm (±7.95 %). They were not calendared, and the porosity of the electrodes was estimated to be 15 % (±2.5 %). The GF/A separator was placed next to the electrode, and the Celgard 2325 next to the metallic sodium to reduce dendrite growth. 70 μL of 1 M $NaPF_6$ in EC:DEC (1:1 V/V) with FEC additive (5.3 wt% FEC) (Flurochem) was used as the electrolyte. Cells were made into CR2032 coin cells. Cells were subjected to an initial 10 mA/g formation cycle, and 15 mA/g for all subsequent cycles. EIS measurements were performed at 2 V, scanning between 10 kHz and 100 mHz. A repeat of at least three cells were made for each test.

3. Results and discussion

To understand the surface and chemical evolution of the active material in air the active material powder was examined by measuring a FTIR spectra every 30 min for 360 min in air, as show in Fig. 1a. The very broad peak at the high frequencies, between ~2500 cm^{-1} and ~3500 cm^{-1}, is indicative of H-bonds, from OH stretching in both hydroxyl groups and absorbed surface water molecules [42]. At ~ 2350 cm^{-1} an asymmetrical double peak is observed, typical of CO_2 [43]. Interestingly, the intensity of this peak does not change over time, suggesting that the absorbed CO_2 is at saturation on the surface. This absorbed CO_2 can react to form carbonates with subsequent reabsorption of. The peaks between 1423 cm^{-1} and 669 cm^{-1} relate to carbonates and hydroxides. Carbonates show a stretching at ~1425 cm^{-1}, typically asymmetrical [44] and hydroxides can show an OH bending at around 1420 cm^{-1} [45]. A comparison of these peaks with pure carbonate (Na_2CO_3 [46] and $NiCO_3$ [47]) and hydroxide compounds (NaOH [47]) is shown in Fig. 1b. The three highlighted regions in Fig. 1b demonstrate the shared peaks, with the bands at ~1423 cm^{-1} and ~879 cm^{-1} being the most observable. It is clear that $NiCO_3$ is not being formed as there is no overlap with the peak at 820 cm^{-1}, despite sharing the peak at ~1434 cm^{-1}. From the broad region of OH stretching between ~2500 cm^{-1} and ~3500 cm^{-1}, as well as peaks at 1422 cm^{-1}, 879 cm^{-1} and 701 cm^{-1}, it is likely that NaOH and Na_2CO_3 is present (Fig. 1b). The spectrum for NaOH shares the very broad region of OH stretching between ~2500 cm^{-1} and ~3500 cm^{-1}, as well as peaks at 1422 cm^{-1}, 879 cm^{-1}, and 701 cm^{-1}. Na_2CO_3 similarly shares peaks at 1429 cm^{-1} and at 878 cm^{-1}.

SEM and EDX (Fig. 2) of the powder shows platelet-like particles existing both singly and as agglomerates. Primary particles are approximately 750 nm × 350 nm × 150 nm in size (as seen in Fig. 2a) with agglomerates being far larger (5–10 μm), as seen in the Fig. 2b. Approximately 500 mg of the active material powder was mounted onto a SEM stub and exposed to the air in an open vial for 3 days, after which acicular particles are observed emanating from the particle agglomerates (Fig. 2b).

From EDS it is observed that the acicular particles contain sodium and oxygen in a 1:1 ratio, with lower levels of the transition metals and carbon (Fig. 2d and e). This indicates that these acicular particles are NaOH, supporting the results of the FTIR analysis.

When the NMST is processed into a slurry, initially a pourable ink is formed, however over time this transforms to a jelly like material as shown in Fig. 3. Initially, just after the electrode slurry has been mixed, it can flow very easily and freely (Fig. 3a). Once the electrode slurry has reached a gel-like state (Fig. 3b) it becomes impossible to coat homogeneously and reliably. A physically stabilised gel can be broken up with increased shear or additional solvent, however if a chemical gel forms this is typically irreversible. One challenge with these time dependent inks is to determine the point at which the ink or slurry becomes uncoatable, often this is determined qualitatively in the laboratory through observation, and in manufacturing through defect observations in the coatings and adhesion properties after or during coating, this leads to potential waste and increased cost [48–51]. For simple slurry cast coatings there is a wide viscosity process window, however with increasing viscosity a change in the viscoelastic properties is also observed. There are several challenges in the measurement of these changes particularly with high solids fraction electrode slurries (>40 wt%) where there is an increase the risk of colloidal jamming. Computational calculations and experimental measurements have shown that this can occur at a solids volume fraction of 54.5% [52].

In this work, gelation has a significant effect upon rheological properties, and the properties are elucidated with time to monitor the onset of different physical and chemical changes in the slurry. Oscillatory rheology was performed to determine the nature of the gelation and to analyse the degree of gelation of the electrode material. Fig. 4a shows the storage, G′ and loss G″, moduli for the

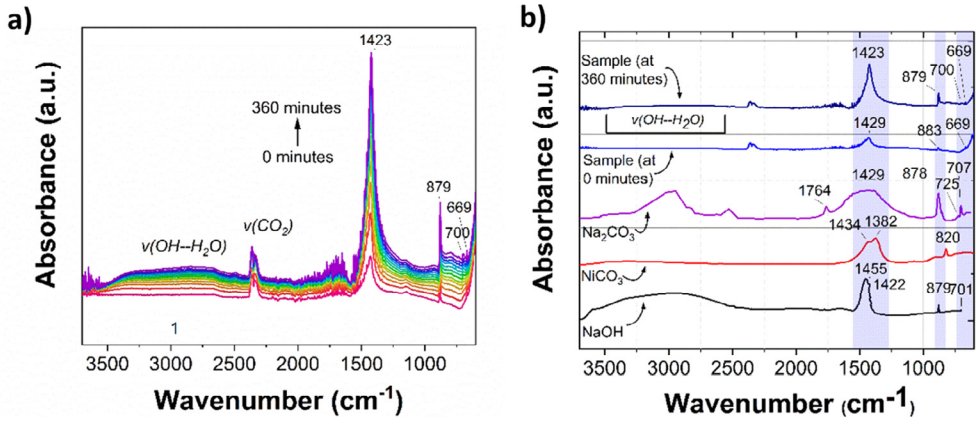

Fig. 1. Ex-situ aging spectra of the carbon-coated active material over 360 min and (b) Comparisons of the spectra with Na_2CO_3,[47] $NiCO_3$,[48] NaOH,[48] and the NaNMST at time 0 and 360 min.

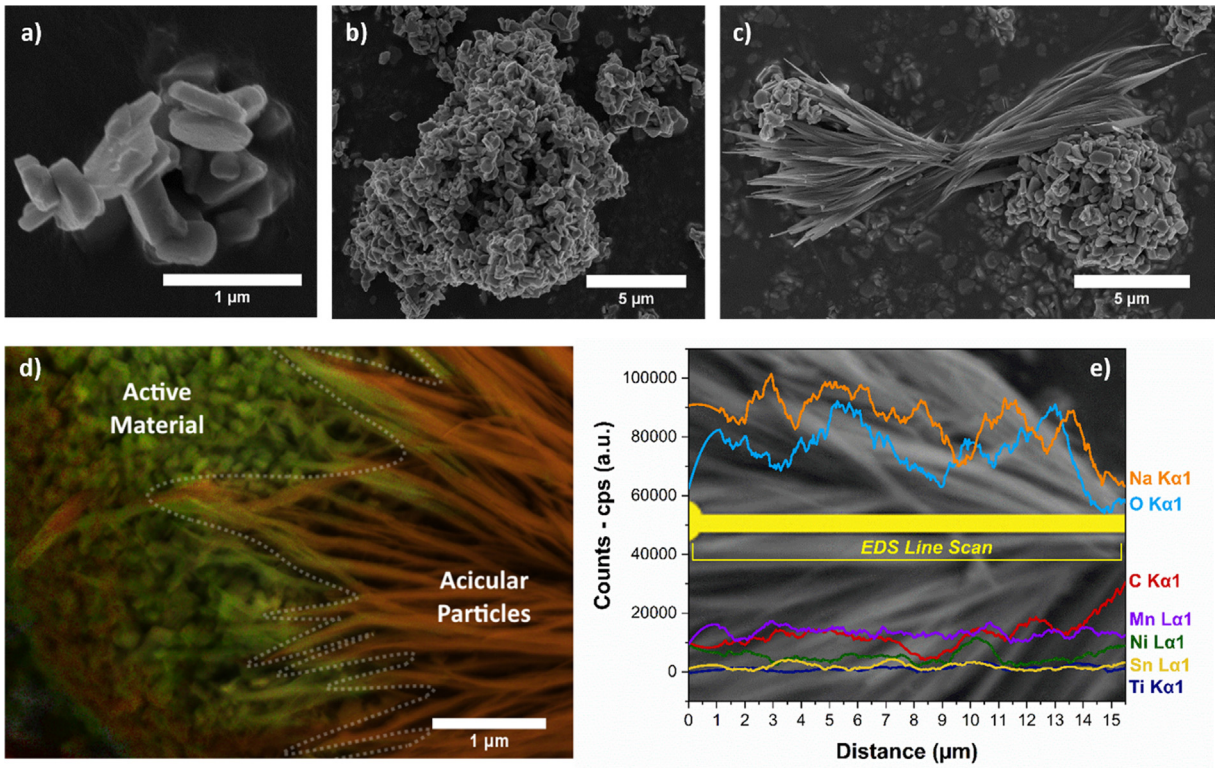

Fig. 2. SEM image of the as synthesised NaNMST material (a) Primary particles, (b) agglomerates, (c) SEM image of the as synthesised NaNMST material after exposure for 3 days, (d) EDS layered spectrum and individual elements, labelled by their elemental chemical.

aging electrode slurry. It can be seen that both G′ and G″ increase over the course of the aging measurements, with a larger increase observed for G′, consistent with the notion of a gelling slurry.

G′ and G″ both demonstrate a convergence of measurements obtained at different frequencies towards the end of the rheological measurements. The convergence is a strong indication of a gel point, GP [53]. As this point of convergence occurs where the viscoelasticity no longer depends on observation time, it is clear that this is not the formation of a physical gel (such as a colloidal glass) but rather a reaction is occurring to form a chemical gel. Rheological indicators of a gel, include the convergence of G′ and G″ in time at different frequencies and the crossover point of G′ and G″, which occurs almost immediately [54]. It should be noted that '0 min' refers to the start of the rheological measurements not the point at which the slurry is mixed (and it does not take into account the transfer time of less than 5 min), it therefore seems logical that there is gelation occurring during the mixing of the electrode slurry. The changes in the phase angle, Fig. 4b, illustrate the balance between the viscous and elastic forces. Initially, the phase angle is at ~40° with slight differences depending on the frequency (or observation time). This indicates a system with a slight dominance towards the storage modulus and the elastic behaviour. This phase angle decreases as the electrode slurry aging progresses, until 65–70 min into the experiment where the convergence occurs, and the phase angle reaches ~1–2°. At this point the gel is realised, and elastic behaviour is almost fully dominant. By the end of the rheological measurements, the physical manifestation of the gel had reached a point where it was completely uncoatable, with properties as shown in the photograph in Fig. 4b.

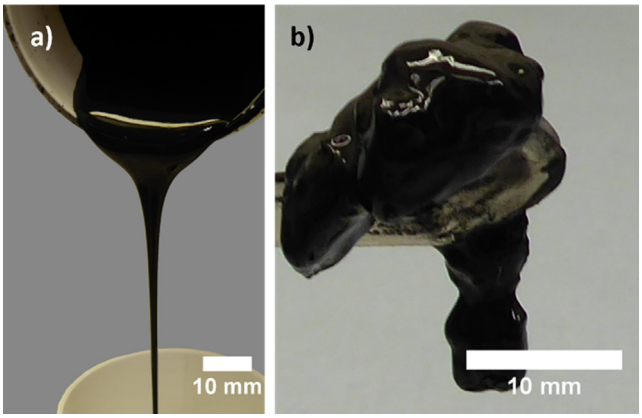

Fig. 3. Comparison between a pristine electrode slurry (a) and the gelled sample (b).

To determine the coatability of the gel, the data was fitted to a two mode Maxwell model using the Reptate software package [55]. Using a Maxwell Model [55,56] the oscillatory data can be fitted with single or multiple modes, each comprised of an elastic, Hookean spring element (E) and a viscous, Newtonian Fluid, dashpot element (η) in series. Multiple modes can be used in parallel to increase the parameters of fitting and improve the quality of fit. In this work one mode per decade of data is used, as shown in Fig. 5 [55].

Relaxation time, τ, is the ratio between the viscous element and the elastic element, as shown in Eq. (1). This is a theoretical property where times much shorter than the relaxation time will behave as a solid (spring), and times longer than the relaxation time will behave as a fluid (dashpot). As stress is equal across a mode and strain is the summed, a rearrangement and differentiation of Hooke's Law and a rearrangement of the Newtonian law of viscosity allows the following equations (Eqs. (2) and (3)) to be written,

$$\tau = \frac{\eta}{E} \tag{1}$$

$$G_a^{'} = E_a \frac{(\omega\tau_a)^2}{1+(\omega\tau_a)^2} \tag{2}$$

$$G_a^{''} = E_a \frac{\omega\tau_a}{1+(\omega\tau_a)^2} \tag{3}$$

where a denotes the mode and ω is the angular frequency of the oscillation.

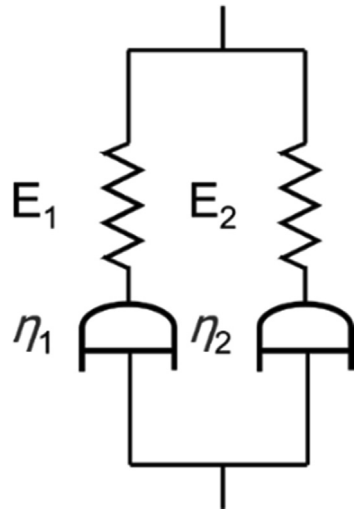

Fig. 5. Two Mode Maxwell Model (sometimes referred to as a Burgers Model).

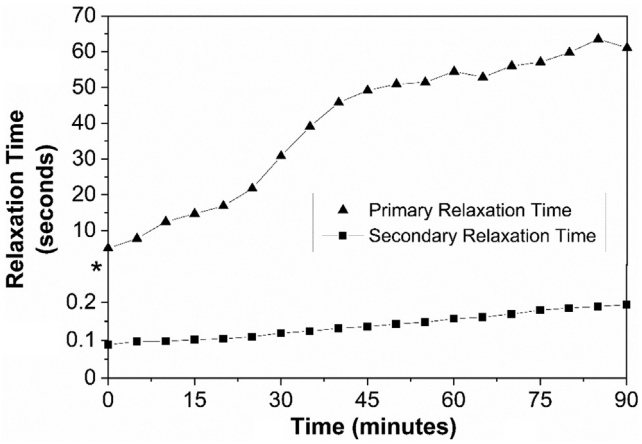

Fig. 6. Primary and Secondary mode relaxation times from the fitted Maxwell Model.

From Fig. 6, it is observed that the primary relaxation time slowly increases for the first 30 min. During this time, the secondary relaxation time is relatively unchanged and upon deformation the electrode slurry will still revert to viscous behaviour relatively quickly. Then, the primary relaxation time rapidly increases indicating that the gelation is rapidly progressing. After

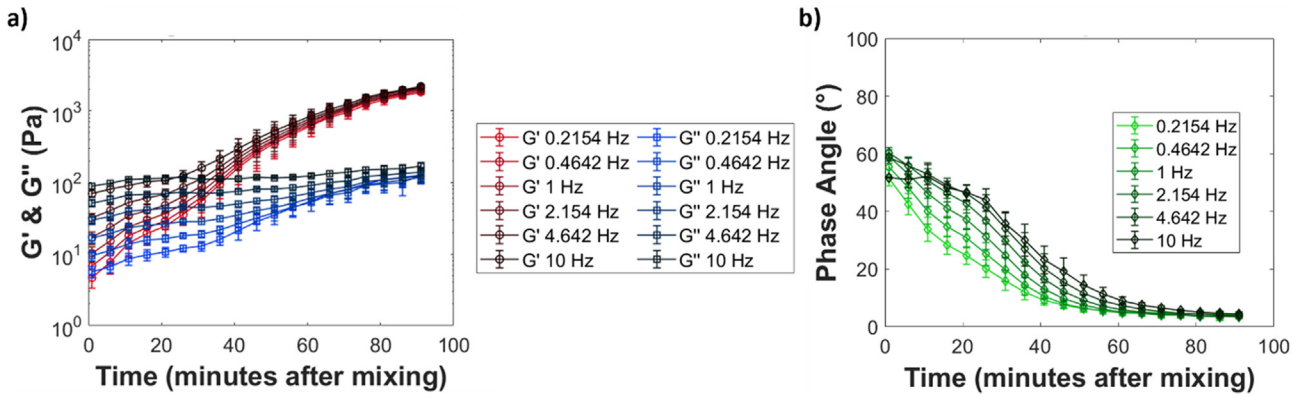

Fig. 4. (a) Storage and Loss Moduli, and (b) Phase Angle for the Aging Electrode Slurry.

45 min, which is suggested as the maximum processing window of this electrode slurry, the rate of primary relaxation time increase drops. The gel structure is formed, with a macromolecule of connected chains throughout the electrode slurry. After this point, the interconnections between chains will strengthen slowly and the gel strength will increase. In terms of the secondary relaxation time, values are much lower, and only change slowly over the period of gelation. The secondary relaxation times denotes the behaviour of the electrode slurry over very short times scales. Below approximately 0.2 s, the secondary relaxation time signifies that the electrode slurries exhibit a strong elastic response, similar to that of a yield stress in a Herschel-Bulkley fluid. Above this secondary relaxation time, the strong elasticity of the electrode slurry partially relaxes, and the primary Maxwell mode elastic response dominates. It is only above the primary relaxation time that the electrode slurry will act fully viscous and flow.

To elucidate the chemical changes which occur during the slurry mixing and ageing, ex-situ FTIR analysis was performed. The main groups relating to water, hydroxide, NMP, PVDF and carbonates are discussed, as shown in Fig. 7. Separate spectra of the individual compounds for comparison can be found in the supplementary information – Fig. S1.

Like that observed on the aged powder, a broad peak at 3442 cm^{-1}, indicative of an OH stretching vibration, is observed. This can be contributed to surface absorbed water in the electrode slurry and from hydrogen bonding throughout the slurry. The increase in the intensity of this peak over time demonstrates that more water is being absorbed as the aging progresses and the amount of hydrogen bonding is similarly increasing. During the course of the ex-situ measurements, the OH stretching peak also experiences a broadening, which is consistent with the increased effects of hydrogen bonding. The very weak shoulder peak at ~3300 cm^{-1}, suggests OH stretching of metal hydroxides, as discussed for the powder FTIR, in Fig. 1, similarly the two peaks at 2361 and 2341 cm^{-1} can be assigned to absorbed CO_2 [43].

The bands located at 3014 cm^{-1} and 2953 cm^{-1} can be assigned to the CH_2 asymmetric and symmetric vibration in NMP.[57] The peak at 2875 cm^{-1} can be attributed the CH stretching in sp^3 hybridised carbons, likely belonging to those in the NMP. 2792 cm^{-1} shows a weak peak that could be assigned to the CH stretching in sp^3 hybridised carbon in NMP. The CH_2 bonds in PVDF would similarly show at these points, however, due to the quantities of NMP and PVDF in the electrode slurries, the contributions due to PVDF would be far smaller. The highest intensity peak belongs to C=O stretching peak. γ-lactams, such as NMP, typically exhibit a stretching at ~1750–1700 cm^{-1} [46]. However, the effect of the methyl group on the nitrogen, over a single hydrogen, causes a greater resonance effect that causes the C=O stretching to shift to lower wavenumbers – ~1670 cm^{-1}, resulting in a wavenumber that is as expected for NMP.

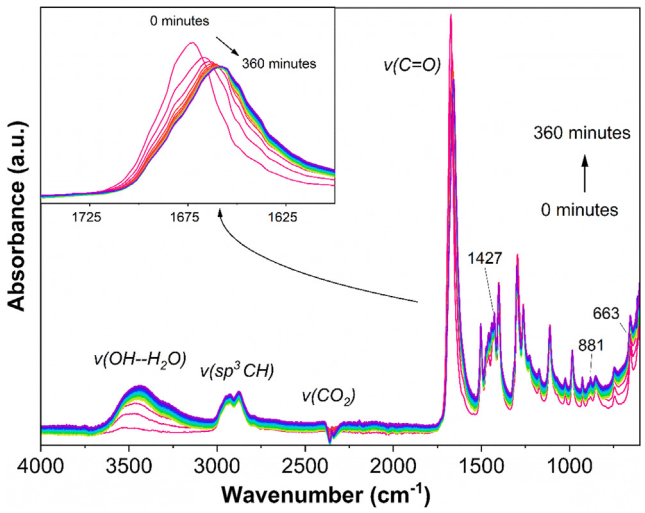

Fig. 7. Ex-situ FTIR Spectra of the Electrode Slurry.

The remaining peaks that have been highlighted, at 1427 cm^{-1}, 881 cm^{-1}, 663 cm^{-1}, are the positions denoting NaOH from the powder FTIR (Fig. 1). Across all these spectra, from 0 to 360 min (Fig. 7), it is very difficult to confidently assign these to NaOH. There is a lot of overlap in these positions with those peaks of NMP (as seen in Fig. S1).

The peaks between 1600 and 1725 have been fitted (Fig. 8). The data shown in Fig. 8 is for scans between 0 and 30 min, later scans are included in the supplementary data. The fitted peaks under this region include: a growing peak at 1617 cm^{-1}, a peak that shifts from 1647 cm^{-1} to 1637 cm^{-1}, a large peak at ~1665 cm^{-1}, a second growing peak at 1681 cm^{-1}, and a final peak at 1691 cm^{-1}. The main peak can be confidently assigned to the C=O bond in the NMP, initially at 1673 cm^{-1} and shifts to lower wavenumbers over time, 1663 cm^{-1} at 30 min. This shift is likely due to hydrogen bonding occurring as water is absorbed into the electrode slurry. Additionally, there is a slight broadening of this peak due to the absorbance of water creating a larger number of environments for this functional group. Secondly, the broad, low intensity peak, initially at 1617 cm^{-1}, can be assigned to conjugated C=C stretching, as has been previously assigned to alkaline treated PVDF in literature [58–60]. As the aging progresses, there appears to be a very slight shift in this peak, along with a slight increase in the intensity, suggesting that there is an increase in the number of these C=C structures within the PVDF as time progresses. Finally, the peak initially lying at 1648 cm^{-1} can also be assigned to non-conjugated C=C structures [60,61]. As the electrode slurry ages, there appears to be a slight shift in this peak, likely due to the effects of hydrogen bonding. There is very little overall change in the intensity of this peak, suggesting that while there may be incremental changes to the amount of non-conjugated C=C structures in the electrode slurry, the overall quantity remains constant, i.e., the rates of production and loss of C=C are equal. Curiously, by comparison of the changes to these two peaks, the quantity of conjugated C=C structures increases while the quantity of non-conjugated C=C structures remains near constant. It can be inferred that the degree of conjugation in the PVDF structure is slowly increasing as the dehydrofluorination reaction progresses. The peak at 1682 cm^{-1}, later at 1681 cm^{-1}, indicates a second C=O stretching occurs, additional to the C=O stretching of NMP. NMP has been previously reported to degrade under basic conditions, causing a ring opening reaction to occur, forming 4-(methylamino) butanoic acid [62]. As the electrode aging progresses, this initially sharp low intensity peak grows in intensity, consistent with a formation of 4-(methylamino) butanoic acid.

Overall, due to the presence of the C=C structures, both conjugated and non-conjugated, evident in the fitted FTIR data, it is likely that a dehydrofluorination reaction of PVDF is occurring. To confirm this the coated and dried electrodes were analysed using XPS. These electrodes (for XPS analysis) were coated immediately after mixing of the electrode slurry and then allowed to dry for ~40 min while exposed to air. This allowed the reaction to occur as the electrodes were drying and, hence, the chemical changes to be observed without the gel network percolating the entire electrode slurry, rendering it completely uncoatable.

Fig. 9 shows the F1s XPS spectra, with three distinct components, two of which relate to the PVDF, while the feature at 684.3 eV can only be assigned to NaF. The presence of NaF can be explained through expulsion of HF from the PVDF structure dur-

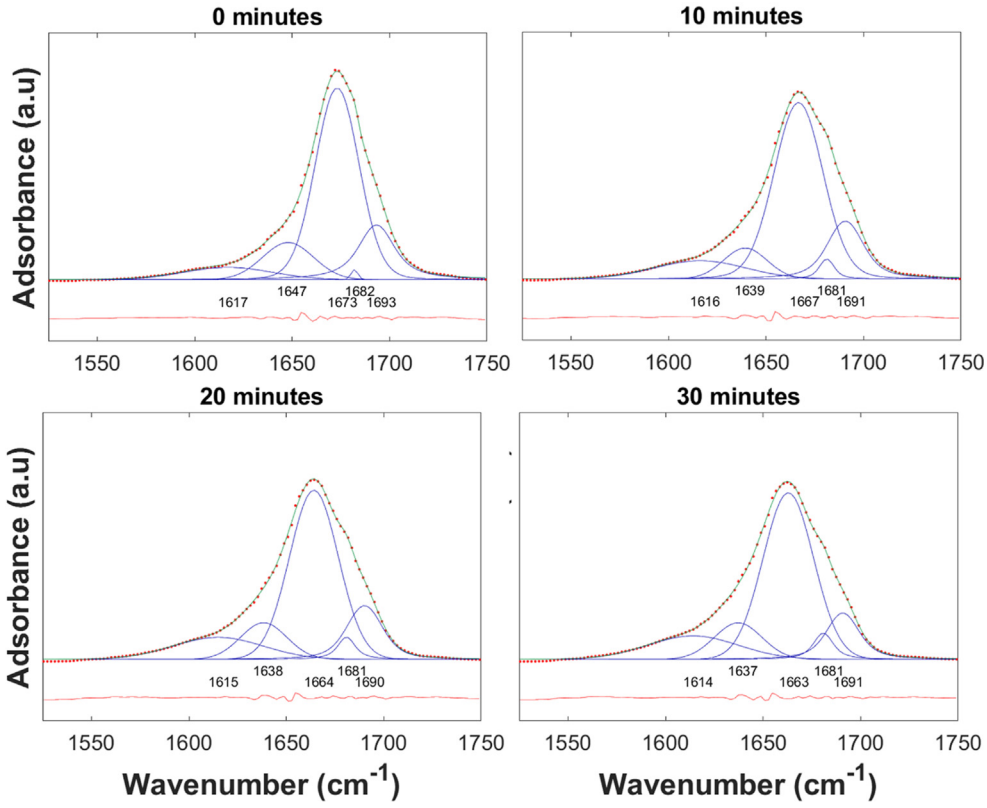

Fig. 8. Fitted Ex-situ FTIR Spectra of the Aging Electrode Slurry between 1525 cm^{-1} and 1750 cm^{-1}.

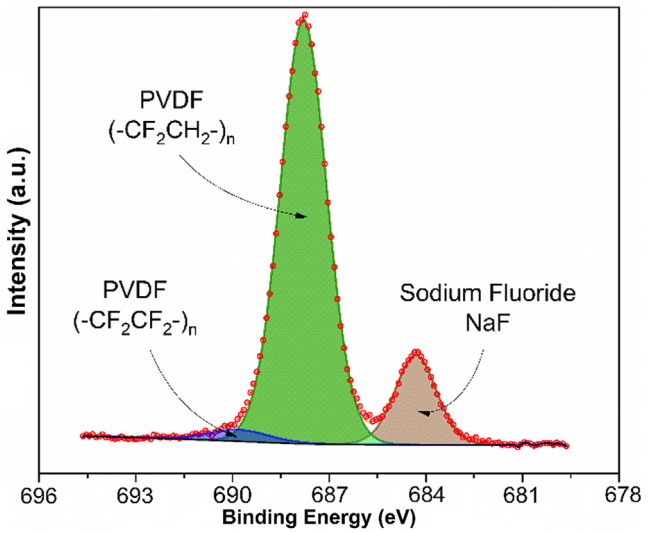

Fig. 9. F1s X-ray Photoemission Spectroscopy of the As-coated Electrode.

ing defluorination, which subsequently reacts with NaOH forming NaF and H_2O, as shown by Eq. (4) (see Fig. 10).

$$NaOH + HF \rightarrow NaF + H_2O \quad (4)$$

By comparison of the XPS peak areas, an elemental quantification can be obtained, and an idea of the degree and progression of the reaction can be noted −81.3% for CF_2CH_2, 3.0% for CF_2CF_2,

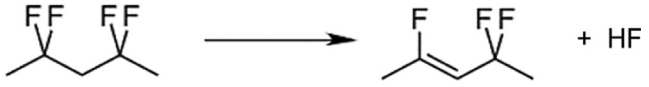

Fig. 10. Dehydrofluorination of PVDF.

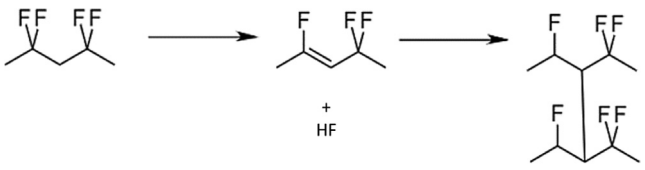

Fig. 11. (a) Electrode coated immediately after mixing. (b) Electrode coated 40 min after mixing.

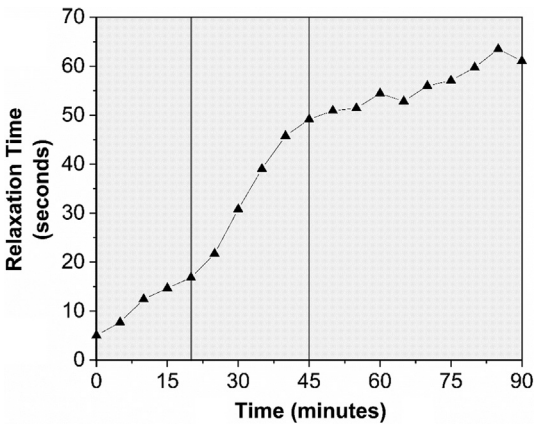

Fig. 12. (a) Half-cell capacity curves for the 1st and 5th cycles for the electrode coated 0 min after mixing. (b) Half-cell capacity vs cycle number for electrodes coated at 0, 20, and 40 min after mixing.

and 15.7 % for NaF Assuming that all of the expelled HF reacts to form NaF, after the aging reaction has been allowed to progress, ~15% of the fluorine in the PVDF was expelled from the polymer

Fig. 13. EIS measured after the formation cycle and after 50 cycles for electrodes coated immediately after mixing, 20 min after mixing, and 40 min after mixing.

and so 15% of the gelled PVDF binder contains conjugated or crosslinked structures.

In summary, NaOH formation on the cathode upon exposure to air has been confirmed from FTIR and SEM analysis, and FTIR and XPS results indicate that a dehydrofluorination reaction of PVDF is occurring during the aging of the slurry. The base catalysed reaction of PVDF in which a carbon–carbon double bond is formed as a result of the elimination of hydrogen fluoride (HF) units from the polymer, as shown in Fig. 14, has been widely reported in PVDF literature previously, although not in battery manufacturing literature [58,64–66]. The formation of these C=C structures allows a crosslinking between PVDF chains to occurs, creating a gel network throughout the electrode ink.

In similar lithium-ion battery systems, it has been shown that LiOH is evolved first, followed by the formation of Li_2CO_3 [36]. It is possible that the formation of LiOH is the cause of gelation in analogous lithium cathode electrode slurries. In this study were unable to detect the presence of Na_2CO_3 and it is possible that the carbonate forms over larger timescales than those used in this research.

The gelation mechanism of dehydrofluorination and subsequent crosslinking is observed also in the time constant for the rheology as indicated through the phase angle, Fig. 4b. The later process, thought to be cross-linking exhibits a ~1–2% phase angle, this observation coupled with the convergence of moduli at frequencies with time indicates the irreversible formation of a chemical gel, as opposed to a physically stabilised gel which can be broken up through increased applied shear. The storage modulus, G′, illustrates changes in the gel structure (Fig. 4a), and the change in G′ with time indictes three likely stages of gel development, as observed in Fig. 15. The first stage is an initially slow rate, whereby the quantities of base are still increasing to the point of saturation and the dehydrofluorination is occurring, but the crosslinking is still slow. The second stage occurs at a faster rate, whereby the highest concentration of C=C structures exists, and crosslinking can readily occur. As this reaction progresses, the quantity of C=C structures decreases until, the third stage where the remaining C=C structures crosslink at a slower rate.

An additional possibility is the hydrolysis and ring opening reaction of NMP which occurs with bases, (Fig. 16) which has been detailed in literature [62,67].

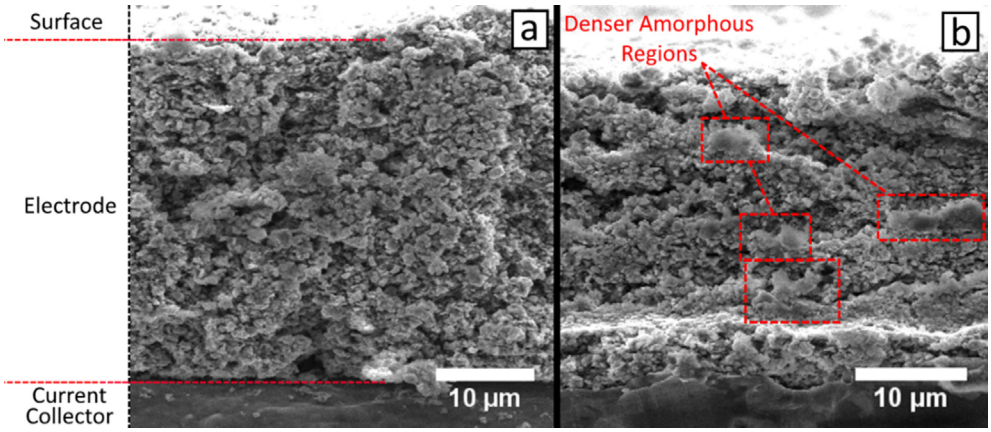

Fig. 14. Dehydrofluorination of PVDF and subsequent crosslinking.

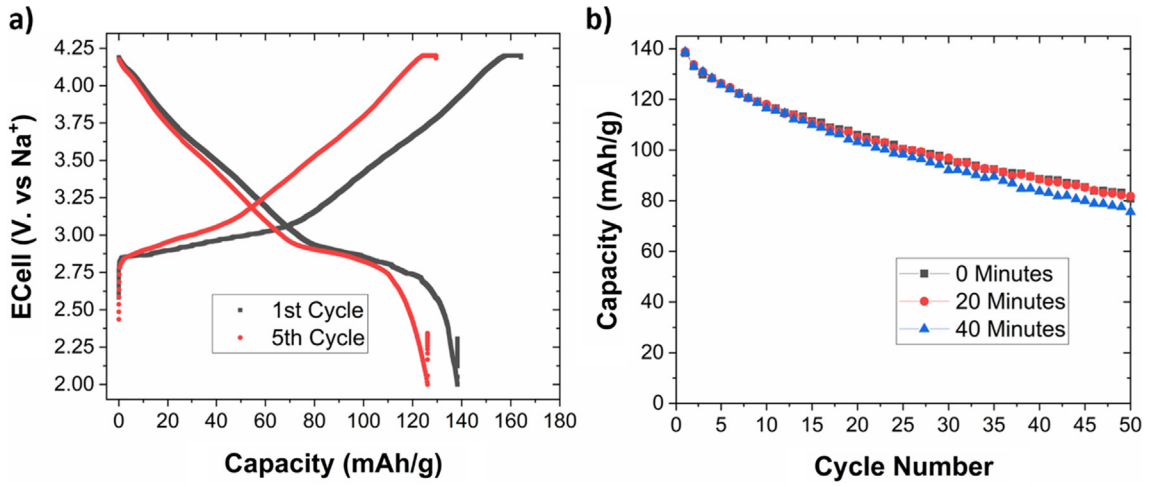

Fig. 15. Primary mode relaxation time, showing the 3 proposed stages of gel development.

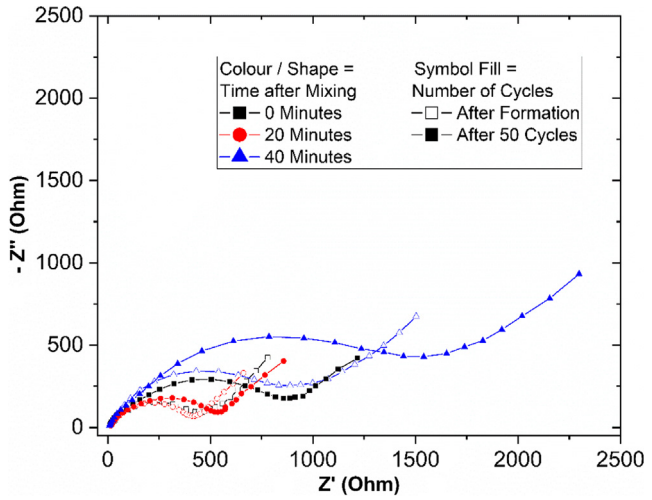

Fig. 16. Hydrolysis and ring opening reaction of NMP, forming 4-(methylamino) butanoic acid.

This reaction occurs with a base present and, by examining the FTIR data in Figs. 7 and 8, there is a suggestion that this reaction is occurring. However, due to the very low intensities of the peaks, the presence of 4-(methylamino) butanoic acid either cannot be confirmed, or it exists in very small quantities. Thus, it likely does not contribute significantly to the gelation of these electrode slurries.

To investigate the effect of the electrode slurry aging upon electrochemical performance, electrodes were coated at different intervals after the mixing was completed, with electrode coating at 40 min being just possible. Beyond this time the electrode slurry was too solid-like to coat. The resulting cross-sectional SEM images of the electrodes are shown in Fig. 11. Fig. 11a shows the image of an electrode coated immediately after mixing, and (b) after 40 min. These samples contained no additives. It can be observed that the longer time resulted in aluminium rich amorphous regions, (Figs. S3 and S4) which are likely caused by aluminium corrosion of the current collector in these basic conditions. The aluminium corrosion will also result in hydrogen production, causing additional micro porosity in the electrodes [63].

Fig. 12a shows the capacity curves for the material in a half cell setup for the first and fifth cycles. It is evident that there is a charge transfer plateau at ~2.8 V, which can be clearly seen for the charge and discharge curves in the first cycle.

There are, however, notable changes due to the electrode slurry aging, as seen in Fig. 12b. Over 50 cycles, the capacity of the material reduces from ~138 ± 1.5 mAh/g to ~81 ± 1.8 mAh/g (averages and standard deviations calculated from no less than 3 cells). The formation of NaOH due to the surface reactions of the active material (Figs. 1 and 2), causes a loss of sodium, the charge carrier, from the active material which leads to a reduction in the capacity of the cells. Coating after 20 min mixing, results in very little change in cycle-life, indicating that the chemical changes due in the electrode slurry at this point are not enough to affect the life of the electrode. Coating after 40 min of mixing, however, results in a steady reduction in capacity from ~138 ± 1.7 mAh/g to ~75 ± 1.8 mAh/g over the 50 cycles.

Electrochemical impedance spectroscopy has been performed as the electrodes have cycled (Fig. 13). It is observed that the charge transfer resistance increases after formation up to 20 min, and then increases significantly after 40 min. This is consistent with the 20-minute stability window of the electrode slurry as observed in the oscillatory rheology (Fig. 13). After 50 cycles the aged slurry charge transfer resistance increases significantly, indicating that the ageing of the slurry influences the surface properties of the material, likely from sodium leaching and resistive sodium residuals at the surface, and hence increases the resistance for sodium transfer across the surface.

4. Conclusions

The powder stability of O3- type high nickel-based sodium ion cathode materials ($NaNi_{1/2}Mn_{1/4}Ti_{1/8}Sn_{1/8}O_2$) and the chemical gelation with PVDF and NMP binder in electrode slurries has been investigated through in-depth chemical analysis, electrochemical cycling, impedance spectroscopy and in-depth time dependent rheological studies of the electrode slurries. $NaNi_{1/2}Mn_{1/4}Ti_{1/8}Sn_{1/8}O_2$, a O3-type layered oxide material, prepared by a solid-state. The effects of air were characterized using FTIR and SEM, and sodium hydroxide was observed over prolonged exposure. The pristine powder was then processed into a slurry with PVDF binder and NMP solvent where over a prolonged time, an irreversible or chemically bonded gel was formed. FTIR studies on the electrode slurries show a formation of C=C bonds during the gelation process. Furthermore, sodium fluoride, observed through XPS in the electrode slurries after mixing and gelation, demonstrates a reaction between sodium hydroxide from the layered oxide and fluorine from the PVDF. These indicate a dehydrofluorination reaction of PVDF. The gelation of the electrode slurry, and the surface reactions affect the electrochemical performance. Al based amorphous regions, formed due to the basicity of the electrode slurry, were detected using cross-sectional SEM and EDS in electrodes coated 40 min after mixing. Electrochemical testing in sodium-metal anode half-cells with coatings produced 0, 20, and 40 min after mixing showed limited initial capacity differences, however, after 50 cycles, an increased capacity decline was observed for electrodes coated after 40 min of mixing. Electrodes coated 40 min after mixing similarly demonstrate greater charge transfer resistances over those produced 0, and 20 min after mixing, which increase further with cycling.

These key findings demonstrate defluorination and cross-linking reactions of the PVDF binder material, caused by the alkalinity of the sodium layered oxide electrode slurries, which in turn cause the gelation of the inks. From the time dependent rheological studies, the new concept of a three-stage gelation process of the electrode slurry was observed, likely linked to the concentration of unsaturated structures in the PVDF. First the PVDF is defluorinated, which causes cross-linking of the chains, which in turn causes a non-reversible chemical gelation of the slurry. Al-rich amorphous regions, observed using cross-section SEM, further emphasises this 3-stage gelation process, and highlight the impact of these reactions on the electrode structure. To predict the coatability from the rheological data would save significant time and cost for electrode development. These observations, indicate a 20-min processing window, which is impractical for manufacturing where 2–4 h or longer electrode slurry stability is required. Accordingly, methods to prevent the surface residue formation, to improve the stability window and prevent basic electrode slurries are required.

To improve the stability and cycling performance of these highly alkaline oxides, changes in the methodology for mixing and coating are required. The major challenges with electrode materials remains the gelation, and the affect this has on the coatability. Suppression of this gelation would mean this material or analogous materials (for both sodium and lithium-ion batteries) may be more freely tested, examined, and optimised. One potential solution, and a possible avenue for future work, is to coat the surface of these electrode materials with a sacrificial or blocking material to prevent exposure to air, and therefore preventing

sodium surface species from forming. An alternative solution is use of an additive in these electrode slurries that is able to absorb water or pacify the surface.

In conclusion this work shows the mechanism for instability of high nickel containing powders and electrode slurries, and presents a new time dependent oscillatory rheology test that can be used to determine the process window for these unstable slurry systems.

CRediT authorship contribution statement

Samuel Roberts: Conceptualization, Methodology, Writing–original draft. **Lin Chen:** Resources, Data curation, Investigation. **Brij Kishore:** Resources, Data curation, Investigation. **Claire E.J. Dancer:** Supervision. **Mark J.H. Simmons:** Methodology, Supervision. **Emma Kendrick:** Conceptualization, Methodology, Supervision.

Declaration of Competing Interest

The authors declare that they have no known competing financial interests or personal relationships that could have appeared to influence the work reported in this paper.

Acknowledgements

SR acknowledges EPSRC for a Doctoral Training Partnership Award (EP/N509796/1) for his PhD at the University of Warwick. EK and MS acknowledge Faraday Institution (EP/S003053/1) and its project Nextrode (FIRG015). EK, LC and BK acknowledge Horizon 2020 European Union funding for research and innovation (GA No. 963542). The authors would like to acknowledge the help of Dr Marc Walker and the use of the Photoemission RTP at the University of Warwick for collecting the XPS data, Dr Tanveer Pathan for his assistance in the XPS analysis, Dr Dominika Gastol for her help in the collection of SEM/EDS data, and Dr Pengcheng Zhu for his assistance in the collection of the cross-sectional SEM/EDS data.

Appendix A. Supplementary material

Supplementary data to this article can be found online at https://doi.org/10.1016/j.jcis.2022.07.033.

References

[1] Y. Zheng, Y. Wang, Y. Lu, Y.S. Hu, J. Li, A high-performance sodium-ion battery enhanced by macadamia shell derived hard carbon anode, Nano Energy 39 (June) (2017) 489–498.
[2] B. Scrosati, J. Garche, Lithium batteries: Status, prospects and future, J. Power Sources 195 (9) (2010) 2419–2430.
[3] M.Á. Muñoz-Márquez, D. Saurel, J.L. Gómez-Cámer, M. Casas-Cabanas, E. Castillo-Martínez, T. Rojo, Na-Ion batteries for large scale applications: a review on anode materials and solid electrolyte interphase formation, Adv. Energy Mater. 7(20) (2017).
[4] Y. Liang, W.-H. Lai, Z. Miao, S.-L. Chou, Nanocomposite materials for the sodium-ion battery: a review, Small 14 (5) (2017) 1702514.
[5] S. Roberts, E. Kendrick, The re-emergence of sodium ion batteries: testing, processing, and manufacturability, Nanotechnol. Sci. Appl. 11 (2018) 23–33.
[6] M.J. Aragón, P. Lavela, G. Ortiz, R. Alcántara, J.L. Tirado, Nanometric P2-Na2/3Fe1/3Mn2/3O2with controlled morphology as cathode for sodium-ion batteries, J. Alloys Compd. 724 (2017) 465–473.
[7] A. Abouimrane et al., Sodium insertion in carboxylate based materials and their application in 3.6 V full sodium cells, Energy Environ. Sci. 5 (11) (2012) 9632.
[8] I. Hasa, S. Passerini, J. Hassoun, A rechargeable sodium-ion battery using a nanostructured Sb–C anode and P2-type layered Na0.6Ni0.22Fe0.11Mn0.66O2 cathode, RSC Adv. 5 (60) (2015) 48928–48934.
[9] Q. Wang et al., Unlocking anionic redox activity in O3-type sodium 3d layered oxides via Li substitution, Nat. Mater. 20 (2021) 353–361.
[10] M. Kouthaman, K. Kannan, P. Arjunan, T. Meenatchi, R. Subadevi, M. Sivakumar, Novel layered O3-NaFe0.45Co0.45Ti0.1O2 cathode material for sodium batteries, Mater. Lett. 276 (2020) 128181.
[11] I. Moeez, D. Susanto, G. Ali, H.G. Jung, H.D. Lim, K.Y. Chung, Effect of the interfacial protective layer on the NaFe0.5Ni0.5O2cathode for rechargeable sodium-ion batteries, J. Mater. Chem. A 8 (28) (2020) 13964–13970.
[12] S. Demirel et al., Growth mechanism and magnetic and electrochemical properties of Na0.44MnO2 nanorods as cathode material for Na-ion batteries, Mater. Charact. 105 (2015) 104–112.
[13] Z. Jian et al., Carbon coated Na3V2(PO4)3 as novel electrode material for sodium ion batteries, Electrochem. commun. 14 (1) (2012) 86–89.
[14] Y. Wang et al., Emerging non-lithium ion batteries, Energy Storage Mater. 4 (2016) 103–129.
[15] W. Tang et al., Highly stable and high rate-performance Na-Ion batteries using polyanionic anthraquinone as the organic cathode, ChemSusChem 12 (10) (2019) 2181–2185.
[16] Y. Liu, G. Wei, M. Ma, Y. Qiao, Role of acid in tailoring prussian blue as cathode for high-performance sodium-ion battery, Chem. – A Eur. J. 23 (63) (2017) 15991–15996.
[17] H. Ye et al., Iron-based sodium-ion full batteries, J. Mater. Chem. A 4 (5) (2016) 1754–1761.
[18] Q. Wang, S. Chu, S. Guo, Progress on multiphase layered transition metal oxide cathodes of sodium ion batteries, Chinese Chem. Lett. 31 (9) (2020) 2167–2176.
[19] C. Zhao et al., Revealing high Na-content P2-type layered oxides as advanced sodium-ion cathodes, J. Am. Chem. Soc. 142 (12) (2020) 5742–5750.
[20] J.-Y. Hwang, S.-T. Myung, Y.-K. Sun, Sodium-ion batteries: present and future, Chem. Soc. Rev. 46 (12) (2017) 3529–3614.
[21] P.F. Wang et al., Ti-substituted NaNi0 5Mn0 5-xTixO2 cathodes with reversible O3 P3 phase Transition.pdf, Adv. Mater. 29 (19) (2017) 1–7.
[22] E. Kendrick et al., Tin containing compounds, WO 2015177568 (A1) (2015) 1–89.
[23] M.H. Han, E. Gonzalo, G. Singh, T. Rojo, A comprehensive review of sodium layered oxides: powerful cathodes for Na-ion batteries, Energy Environ. Sci. 8 (1) (2015) 81–102.
[24] Y.K. Sun, Direction for commercialization of O3-type layered cathodes for sodium-ion batteries, ACS Energy Lett. 5 (4) (2020) 1278–1280.
[25] J.Y. Hwang, S.T. Myung, D. Aurbach, Y.K. Sun, Effect of nickel and iron on structural and electrochemical properties of O3 type layer cathode materials for sodium-ion batteries, J. Power Sources 324 (2016) 106–112.
[26] K. Smith, J. Treacher, D. Ledwoch, P. Adamson, E. Kendrick, Novel high energy density sodium layered oxide cathode materials: from material to cells, ECS Trans. 75 (22) (2017) 13–24.
[27] J. Xu et al., Understanding the degradation mechanism of lithium nickel oxide cathodes for li-ion batteries, ACS Appl. Mater. Interfaces 8 (2016) 31677–31683.
[28] J.-Y. Hwang, S.-T. Myung, J.U. Choi, C.S. Yoon, H. Yashiro, Y.-K. Sun, Resolving the degradation pathways on O3-type layered oxides cathode surface through the nano-scale aluminum oxide coating for high-energy density sodium-ion batteries, J. Mater. Chem. A 5 (2017) 23671–23680.
[29] M. Biso, R. Colombo, M.-J. Uddin, M. Stanga, S.-J. Cho, A rheological behavior of various polyvinylidene difluoride binders for high capacity LiNi0.6Mn0.2Co0.2O2, Engineering 47 (2007) 21–25.
[30] J.E. Marshall et al., On the solubility and stability of polyvinylidene fluoride, Polymers (Basel) 13 (9) (2021) 1–31.
[31] J.M. Paulsen, H. Park, Y.H. Kwon, Process of making cathode material containing Ni-based lithium transition metal oxide, US8574541B2, 2013.
[32] H. Park, S.S. Shin, S.Y. Park, H.S. Shin, J.M. Paulsen, Method of preparing material for lithium secondary battery of high performance, US8540961B2, 2013.
[33] E. De La Llave et al., Comparison between Na-Ion and Li-Ion cells: understanding the critical role of the cathodes stability and the anodes pretreatment on the cells behavior, ACS Appl. Mater. Interfaces 8 (3) (2016) 1867–1875.
[34] T. Li, X.-Z. Yuan, L. Zhang, D. Song, K. Shi, C. Bock, Degradation Mechanisms and Mitigation Strategies of Nickel-Rich NMC-Based Lithium-Ion Batteries, Springer, Singapore, vol. 3(1), 2020.
[35] R. Jung et al., Effect of ambient storage on the degradation of ni-rich positive electrode materials (NMC811) for li-ion batteries, J. Electrochem. Soc. 165 (2) (2018) A132–A141.
[36] Y. Su et al., Strategies of removing residual lithium compounds on the surface of Ni-rich cathode materials†, Chinese J. Chem. 39 (1) (2021) 189–198.
[37] C. Busà, M. Belekoukia, M.J. Loveridge, The effects of ambient storage conditions on the structural and electrochemical properties of NMC-811 cathodes for Li-ion batteries, Electrochim. Acta 366 (2021).
[38] Z. Chen et al., The high-temperature and high-humidity storage behaviors and electrochemical degradation mechanism of LiNi0.6Co0.2Mn0.2O2 cathode material for lithium ion batteries, J. Power Sources 363 (2017) 168–176.
[39] P. Teichert, G.G. Eshetu, H. Jahnke, E. Figgemeier, Degradation and aging routes of ni-rich cathode based li-ion batteries, Batteries 6 (1) (2020) 1–26.
[40] W.M. Seong, Y. Kim, A. Manthiram, Impact of residual lithium on the adoption of high-nickel layered oxide cathodes for lithium-ion batteries, Chem. Mater. 32 (22) (2020) 9479–9489.
[41] N.N. Loginova, L.Y. Madorskaya, N.K. Podlesskaya, Relations between the thermal stability of partially fluorinated polymers and their structure, Polym. Sci. U.S.S.R. 25 (12) (1983) 2995–3000.

[42] M. Taibi, S. Ammar, N. Jouini, F. Fiévet, P. Molinié, M. Drillon, Layered nickel hydroxide salts: synthesis, characterization and magnetic behaviour in relation to the basal spacing, J. Mater. Chem. 12 (11) (2002) 3238–3244.
[43] F. Rolle, M. Sega, Use of FTIR spectroscopy for the measurement of CO 2 carbon stable isotope ratios, in: 19th International Congress of Metrology, vol. 05002, 2019, pp. 1–6.
[44] S. Campbell, K.M. Poduska, Incorporating far-infrared data into carbonate mineral analyses, Minerals 10 (7) (2020) 1–11.
[45] H. Zhang, H. Ming, W. Zhang, G. Cao, Y. Yang, Coupled carbonization strategy toward advanced hard carbon for high-energy sodium-ion battery, ACS Appl. Mater. Interf. 9 (28) (2017) 23766–23774.
[46] P.J. Linstrom, W.G. Mallard (Eds.), NIST Chemistry WebBook, NIST Standard Reference Database Number 69, 20899th ed. Gaithersburg MD: National Institute of Standards and Technology, 2022.
[47] J.W. Sons, I. SpectraBase, "SpectraBase, 2022. <https://spectrabase.com/about> (accessed: 2022-02-15).
[48] J. Park, K. Shin, C. Lee, Improvement of cross-machine directional thickness deviation for uniform pressure-sensitive adhesive layer in roll-to-roll slot-die coating process, Int. J. Precis. Eng. Manuf. 16 (5) (2015) 937–943.
[49] Z. Qiao, Z. Wang, C. Zhang, S. Yuan, Y. Zhu, J. Wang, PVAm–PIP/PS composite membrane with high performance for CO_2/N_2 separation, AIChE J. 59 (4) (2012) 215–228.
[50] J. Wang, Q. Mao, Methodology based on the PVT behavior of polymer for injection molding, Adv. Polym. Technol. 32 (2013) (2012) 474–485.
[51] C.D. Reynolds, P.R. Slater, S.D. Hare, M.J.H. Simmons, E. Kendrick, A review of metrology in lithium-ion electrode coating processes, Mater. Des. 209 (2021) 109971.
[52] W.C.K. Poon, Colloidal glasses, MRS Bull. (February) (2004) 96–99.
[53] F. Chambon, H.H. Winter, Linear viscoelasticity at the gel point of a crosslinking PDMS with Imbalanced Stoichiometry, J. Rheol. (N.Y.N.Y) 31(8) (1987) 683–697.
[54] H.H. Winter, Can the gel point of a cross-linking polymer be detected by the G' – G" crossover?, Polym Eng. Sci. 27 (22) (1987) 1698–1702.
[55] V.A.H. Boudara, D.J. Read, J. Ramírez, Reptate rheology software: Toolkit for the analysis of theories and experiments, J. Rheol. (N. Y. N. Y) 64(3) (2020) 709–722.
[56] T. Venerová, M. Pekař, Rheological properties of gels formed by physical interactions between hyaluronan and cationic surfactants, Carbohydr. Polym. 170 (2017) 176–181.
[57] H. Bai, X. Wang, Y. Zhou, L. Zhang, Preparation and characterization of poly (vinylidene fluoride) composite membranes blended with nano-crystalline cellulose, Prog. Nat. Sci. Mater. Int. 22 (3) (2012) 250–257.
[58] G.J. Ross, J.F. Watts, M.P. Hill, P. Morrissey, Surface modification of poly (vinylidene fluoride) by alkaline treatment: 1. The degradation mechanism, Polymer (Guildf) 41 (5) (2000) 1685–1696.
[59] L. Xiao, D.M. Davenport, L. Ormsbee, D. Bhattacharyya, Polymerization and functionalization of membrane pores for water related applications, Ind. Eng. Chem. Res. 54 (2015) 4174–4182.
[60] M.F. Rabuni, N.M. Nik Sulaiman, M.K. Aroua, N.A. Hashim, Effects of alkaline environments at mild conditions on the stability of PVDF membrane: an experimental study, Ind. Eng. Chem. Res. 52 (45) (2013) 15874–15882.
[61] D. Li, M. Liao, Dehydrofluorination mechanism, structure and thermal stability of pure fluoroelastomer (poly(VDF-ter-HFP-ter-TFE) terpolymer) in alkaline environment, J. Fluor. Chem. 201 (August) (2017) 55–67.
[62] Y.J. Ou, X.M. Wang, C.L. Li, Y.L. Zhu, X.L. Li, The Effects of Alkali and Temperature on the Hydrolysis Rate of N-methylpyrrolidone, IOP Conf. Ser. Earth Environ. Sci. 100 (2017) 012036.
[63] P. Zhu, D. Gastol, J. Marshall, R. Sommerville, V. Goodship, E. Kendrick, A review of current collectors for lithium-ion batteries, J. Power Sources 485 (2021).
[64] H. Kise, H. Ogata, Phase transfer catalysis in dehydrofluorination of poly (vinylidene fluoride) by aqueous sodium hydroxide solutions, J. Polym. Sci. A1. 21 (12) (1983) 3443–3451.
[65] D.M. Brewis, I. Mathieson, I. Sutherland, R.A. Cayless, R.H. Dahm, Pretreatment of poly(vinyl fluoride) and poly(vinylidene fluoride) with potassium hydroxide, Int. J. Adhes. Adhes. 16 (2) (1996) 87–95.
[66] A. Taguet, B. Ameduri, B. Boutevin, Crosslinking of vinylidene fluoride-containing fluoropolymers, Adv. Polym. Sci. 184 (July) (2005) 127–211.
[67] D.A. Wells, H.F. Thomas, G.A. Digenis, Mutagenicity and cytotoxicity of N-methyl-2-pyrrdidinone and 4-(Methy1amino) butanoic acid in the salmonella/microsome assay, J. Appl. Toxicol. 8 (2) (1988) 135–139.